

**View Article Online PAPER** 



Cite this: Phys. Chem. Chem. Phys., 2019, 21, 15080

Received 31st May 2019, Accepted 7th June 2019

DOI: 10.1039/c9cp03105g

rsc.li/pccp

# Tuning the electronic properties of the γ-Al<sub>2</sub>O<sub>3</sub> surface by phosphorus doping†

Muhammed Acikgoz, # M. Reza Khoshi, # Jaren Harrell, Alessandro Genova, Rupali Chawla, Huixin He\* and Michele Pavanello\*§

Tuning the electronic properties of oxide surfaces is of pivotal importance, because they find applicability in a variety of industrial processes, including catalysis. Currently, the industrial protocols for synthesizing oxide surfaces are limited to only partial control of the oxide's properties. This is because the ceramic processes result in complex morphologies and a priori unpredictable behavior of the products. While the bulk doping of alumina surfaces has been demonstrated to enhance their catalytic applications (i.e. hydrodesulphurization (HDS)), the fundamental understanding of this phenomenon and its effect at an atomic level remain unexplored. In our joint experimental and computational study, simulations based on Density Functional Theory (DFT), synthesis, and a variety of surface characterization techniques are exploited for the specific goal of understanding the structure-function relationship of phosphorus-doped  $\gamma$ -Al<sub>2</sub>O<sub>3</sub> surfaces. Our theoretical calculations and experimental results agree in finding that P doping of  $\gamma$ -Al<sub>2</sub>O<sub>3</sub> leads to a significant decrease in its work function. Our computational models show that this decrease is due to the formation of a new surface dipole, providing a clear picture of the effect of P doping at the surface of  $\gamma$ -Al<sub>2</sub>O<sub>3</sub>. In this study, we uncover a general paradigm for tuning support-catalyst interactions that involves electrostatic properties of doped  $\gamma$ -Al<sub>2</sub>O<sub>3</sub> surface, specifically the surface dipole. Our findings open a new pathway for engineering the electronic properties of metal oxides' surfaces.

## Introduction

Metal oxides and their surfaces find extensive use in numerous fields of materials science, such as chemical catalysis, photocatalysis, and photovoltaics, among others. 1,2 Thus, engineering the electronic properties of the oxide surfaces is crucial for a broad application of materials, as well as for the improvement of their current applications. 1,3 As of today, however, serious limitations affect the extent of this control, mainly for two reasons. First, most synthetic methods yielding well defined doped surfaces are limited to academic use (small scale) - which are not cost effective for industrial applications - or the products are not stable under the operational conditions of most industrial processes. 4 Secondly, the ceramic processes typically employed in industry to engineer oxide-containing materials result in complex morphologies<sup>5</sup> and a priori unpredictable behavior of the generated materials.

Department of Chemistry, Rutgers University, Newark, NJ 07102, USA. E-mail: huixinhe@rutgers.edu, m.pavanello@rutgers.edu

- # These authors contributed equally to the work.
- § Also affiliated to the Physics Department.

In this work, our primary goal is to generate phosphorous doped alumina surfaces, by employing simple ceramic processes and characterizing their electronic properties. We aim at shedding light on three major points: (1) a theory-experiment correlation to inspect the average or the most likely surface morphology (we consider an array of possible locations of P on  $\gamma$ -Al<sub>2</sub>O<sub>3</sub> surfaces); (2) finding a structure–function relationship between the electronic properties and surface morphology. This can be exploited when metal oxides are engineered; and (3) determining the degree of thermodynamic stability for various possible surface terminations, as well as P locations on the P-doped  $\gamma$ -Al<sub>2</sub>O<sub>3</sub> (P- $\gamma$ -Al<sub>2</sub>O<sub>3</sub>).

Our study focuses on an atomic-level understanding of the morphology and the structure-property relationships of realistic (hydroxylated) surfaces of P-γ-Al<sub>2</sub>O<sub>3</sub> nanoparticles. γ-Al<sub>2</sub>O<sub>3</sub> has been widely used as an adsorbent and a catalyst, and also it is perhaps the most important nanomaterial used as a support for metal catalysts.<sup>7</sup> The properties of Al<sub>2</sub>O<sub>3</sub> can change during chemical operations, which include chemical contamination, thermal stress leading to loss of surface area, pore blockage, and undesired crystal phases.<sup>8-10</sup> It has been empirically observed that dopants improve the overall performance of catalysts acting as crystal phases and/or surface area stabilizers. 11-13 For example, studies on the fact that treating the surface of \( \gamma \text{-Al}\_2 O\_3 \) with phosphates could

<sup>†</sup> Electronic supplementary information (ESI) available: Morphology and PDOS data of two P-doped models, as well as small cells and their computed IR spectra. Fundamentals of the PF-KPFM technique and surface-averaged electrostatic potentials. See DOI: 10.1039/c9cp03105g

Paper

largely promote the performance of the catalysts in hydrodesulphurization (HDS) have been reported. 13-15 Also, doping of γ-Al<sub>2</sub>O<sub>3</sub> is commonly used for tuning its mechanical<sup>16,17</sup> and optical properties. 18,19 Many dopants such as metal, silica, and heteroatoms have been used to modify the γ-Al<sub>2</sub>O<sub>3</sub> surface or its bulk during fabrication. 20-23 Phosphorus is our choice of dopant, because it has a variety of atomic coordinations and multiple electronic states. Also, it is known that phosphorus can covalently bind to Al<sub>2</sub>O<sub>3</sub>, thus making a stable catalyst support.<sup>24,25</sup>

Experimentally, we characterized the structural and chemical properties of both P-doped and non-doped γ-Al<sub>2</sub>O<sub>3</sub> nanoparticles by utilizing Fourier transform infrared (FT-IR) spectroscopy, solid-state magic-angle spinning nuclear magnetic resonance (MAS-NMR), energy-dispersive X-ray spectroscopy (EDS), and PeakForce Kelvin probe force microscopy (PF-KPFM) techniques. On the theoretical side, we carried out several DFT simulations accounting for an array of surface and doping morphological models. Electronic properties were characterized by computing the density of Kohn-Sham states (DOS), surface work function and surface dipole moment, as well as IR and NMR of P-doped and non-doped  $\gamma$ -Al<sub>2</sub>O<sub>3</sub>.

## Results and discussion

To investigate the P content in the doped γ-Al<sub>2</sub>O<sub>3</sub> structure, EDS was conducted, using EDAX coupled with FE-SEM Hitachi S-4800. As EDAX microprobe analysis is semi-quantitative, analysis of several samples was carried out and the averaged values are presented in Table 1.

We perform DFT calculations (see the computational details section) where γ-Al<sub>2</sub>O<sub>3</sub> and P-γ-Al<sub>2</sub>O<sub>3</sub> surfaces are presented for two different essential surface models, namely oxygen terminated and 100% hydroxylated (OH terminated). We considered single-atom doping and two-atom doping (i.e., two interacting and independent P atoms in the simulation cell). Each structure underwent geometry optimization. Although we carried out the simulations on cells of two sizes (a small bulk unit containing 40 atoms and a bulk supercell containing 160 atoms) the presented results are based on the simulations of the larger, more realistic cell, unless otherwise stated. Both slab models consist of five cation layers (tetrahedrally and octahedrally coordinated Al atoms). A vacuum thickness of 15 Å above the surface was added between two periodically repeated slabs. We placed P on one surface of the slab. The bottom 40% of atoms in each slab was kept fixed at their optimized positions throughout the simulations. We consider four different positions for the P atoms in two categories:

• models sub/surf: P is located on a subsurface/surface site substituting an Al atom;

Table 1 The results of EDS analysis for the P-γ-Al<sub>2</sub>O<sub>3</sub> samples

Element	Weight (%)	Atomic (%)
0	42.8	56.2
Al	48.7	38.0
P	8.5	5.8

• models md/bd: P is in a phosphate-type ligand with mono/ bidentate complexation to a surface Al atom.

Throughout the manuscript, we use abbreviations to identify each surface model of the relevant termination (e.g., O-sub and OH-sub are for subsurface locations of P on O-terminated and OH-terminated surfaces, respectively).

In the simulation, we choose the (001) surface of  $\gamma$ -Al<sub>2</sub>O<sub>3</sub> in the spinel-like bulk morphology proposed by Gutiérrez et al., 26 Pinto et al.,27 and Taniike et al.28 This structure compares favorably to known crystallographic and physical properties of  $\gamma$ -Al<sub>2</sub>O<sub>3</sub>.<sup>29</sup> In Fig. 1 we depict the computed morphology (a and b) for the O-terminated γ-Al<sub>2</sub>O<sub>3</sub> model as well as its associated DOS plot (c). Not surprisingly, this surface termination activates the material. Although it is known that this termination is only detectable at very high temperatures, we present it here as a model for oxygen-rich surface islands.

As our picture of  $\gamma$ -Al<sub>2</sub>O<sub>3</sub> is that of a heterogeneous material with OH-rich and O-rich domains, we also present a depiction of the 100% hydroxylated surface termination of the supercell in Fig. 1(d and e) alongside the associated DOS plot (f). From the mentioned figure, it is clear that, as expected, hydroxylated γ-Al<sub>2</sub>O<sub>3</sub> is an insulator and electronically stable.

Experimentally, the P-γ-Al<sub>2</sub>O<sub>3</sub> was synthesized by impregnation of phosphoric acid and commercially available γ-Al<sub>2</sub>O<sub>3</sub>, followed by a simple and commonly applied ceramic process, i.e. a high temperature annealing process in air (see the experimental details section). By optimizing the ratio of γ-Al<sub>2</sub>O<sub>3</sub> and the molarity of H<sub>3</sub>PO<sub>4</sub>, we are able to tune the doping level of P. In Fig. 2 we show the atomic-level surface morphologies, resulting from the DFT simulations and the corresponding PDOS. When considering phosphate chemisorption, it can be realized through a monodentate or bidentate ligand configuration. Additionally, here we consider two types of slabs: one that is stoichiometric with a P(5+) oxidation state, and one that is consistent with a P(3+) oxidation state. This was accomplished by the addition of an electron donor to the bottom of the slab. The relevant computed morphologies and associated PDOSs can be seen in S1 and S2 (ESI†) for both O-terminated and OH-terminated surface models, where it can be seen that the phosphorous coordination and overall local geometry and surface PDOS are slightly affected by the overall stoichiometry of the slab. This indicates that the chosen slab model is sufficiently thick that the surface properties are resilient to the chemistry occurring at the other end of the slab.

In the models O-sub/O-surf and OH-sub/OH-surf, the P atom was introduced at a tetrahedral Al site. The theoretical prediction delivers a clear picture for O-sub: a planar configuration is assumed for P, consistent with an effective double oxidation (3+ oxidation state). For this model, we also explore the O terminated subsurface doped with two P atoms at the three tetrahedral doping sites (Fig. S3 and S4, ESI†). The three resulting models show how the location of the second P atom introduces significant changes to the shape of the conduction band (CB). As there are unoccupied orbitals with P character, similarly to the previous O terminated P-doped model (O-sub) one or both subsurface P atoms have 3+ oxidation state character.

**PCCP** Paper

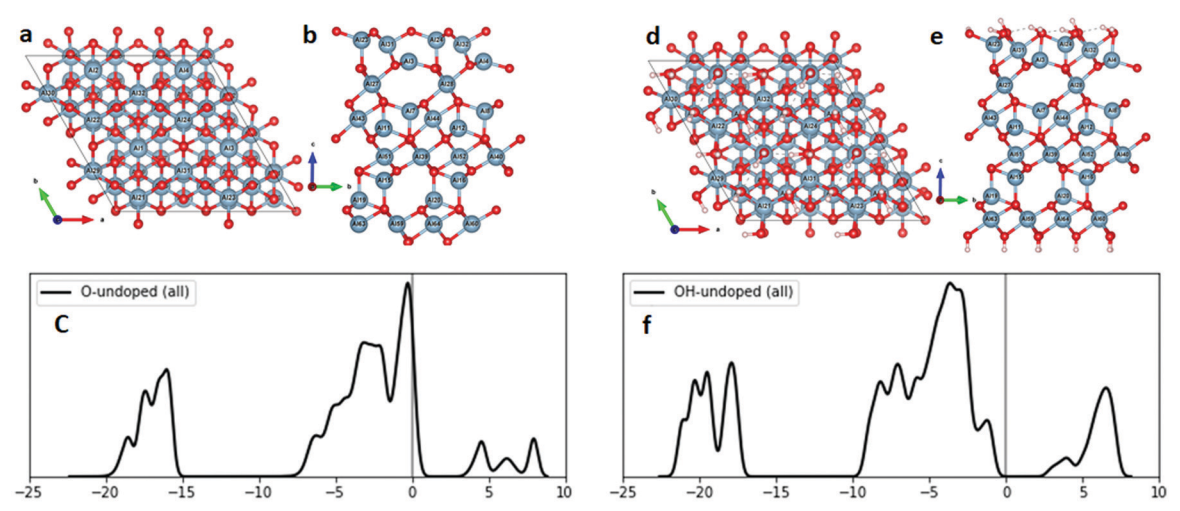


Fig. 1 Computed morphology, both top view (a) and side view (b), and associated DOS (c) of a non-doped O terminated  $\gamma$ -Al<sub>2</sub>O<sub>3</sub> surface. Those of the 100% hydroxylated  $\gamma$ -Al<sub>2</sub>O<sub>3</sub> surfaces are given in (d), (e), and (f), respectively. Fermi energy placed at zero for DOSs.

When the P atom is located on the surface (model O-surf), it causes surface reorganization and distortions across the surface O atoms to form an O-dimer (see the relevant structure in Fig. 2a). The computed PDOS of this model has a band gap of 4 eV and it is shown that the Fermi level lies at the top of the valence band. The computed PDOS plots display no significant changes either in monodentate (O-md) or bidentate (O-bd) configuration models, even though the surface morphology in **O-bd** was affected by several distortions of surface O atoms.

When doping the OH terminated surface, we obtain the morphology/DOS depicted in Fig. 2. In model OH-sub, the P atom is now non-planar, maintaining the lone pair as a partially filled state. At the same time, the P atom is sheltered in a subsurface site. The surface P atom doping (OH-surf model) at the tetrahedral Al site causes the neighboring octahedral Al site to become five coordinated. In this situation, the surface P atom becomes three coordinated (see Fig. S5, ESI†). When considering the phosphate models (OH-md and OH-bd), we notice that the surface largely maintains its non-doped surface morphology (low reorganization), but the DOS profile changes, displaying clear gaps with no P states on the band edges.

We further investigate the subsurface P doping and also consider higher concentration doping (i.e., two independent P atoms in the same simulation cell). The idea behind this set of simulations is to inspect the extent of nonadditivity/cooperation in the electronic behavior of the surfaces after P-doping. We achieved this by replacing another tetrahedral Al with P. The second P was inserted at three of the different, available and inequivalent tetrahedral Al locations and considered both the OH and O terminated surfaces. For the OH terminated surface, we found two local minima of the potential energy surface. The first structure features one P atom four-coordinated with three subsurface oxygen atoms and one surface hydroxyl group. The second P location is 3 coordinated with its lone pair still on P and points in the direction of the spinel defect site (Fig. S6a, ESI†). In the second local minimum structure, the P closer to the surface moved toward the bulk expelling a water molecule

(Fig. S6b, ESI†). When the O-terminated surface is considered, the two P atoms achieve a planar tri-coordinated geometry. Conceivably, this is an indication that the oxidation state of P atoms is now 3+.

The PDOS of these surfaces showed largely the same trend as for singly doped surfaces. For the O-terminated surfaces, P doping induces narrowing of the gap and the appearance of states with P character at the band edges. The OH-terminated surfaces are more resilient to the doping and maintain a large gap. However, as in the case of the singly doped surface, the valence band (VB) edge has a strong P character (Fig. S7, ESI†). Thus, we do not find a significant cooperative effect between P sites.

Our next set of investigations is regarding the simulations and measurement of the work function (WF or  $\phi$ ) of P doped and non-doped γ-Al<sub>2</sub>O<sub>3</sub> nanoparticles. To understand the influence of P doping on the work function of γ-Al<sub>2</sub>O<sub>3</sub> nanoparticles, PeakForce Kelvin probe force microscopy (PF-KPFM™) in an argonfilled glovebox is conducted for both doped and non-doped γ-Al<sub>2</sub>O<sub>3</sub> nanoparticles (see S8 for more details, ESI†). PF-KPFM measurement is carried out on several nanoparticles with similar dimensions for each sample (Fig. 3).

The average measured WF of  $\gamma$ -Al<sub>2</sub>O<sub>3</sub> is 4.88  $\pm$  0.04 eV, while the average measured WF of P- $\gamma$ -Al<sub>2</sub>O<sub>3</sub> is 4.16  $\pm$  0.06 eV. Our results show that doping of  $\gamma$ -Al<sub>2</sub>O<sub>3</sub> by phosphorus has lowered its WF by almost 15% (Fig. 4a).

We employ and compare GGA with GGA+U for the calculation of the WFs of all surface models. When performing GGA+Uwe derive suitable U values for O (1.11 eV) and P (1.77 eV) by employing the Cococcioni-de Gironcoli linear response method30 to the small surface structures (40 atoms). DFT+U is chosen here to remove the spurious self-interaction present in semilocal (GGA) exchange-correlation functionals31 and is particularly suited to improve the ab initio description of surfaces and interfaces.

The corresponding surface-averaged electrostatic potential of each model is plotted as a function of distance from the surface (Fig. in S9, ESI†). The values of WFs and the corresponding

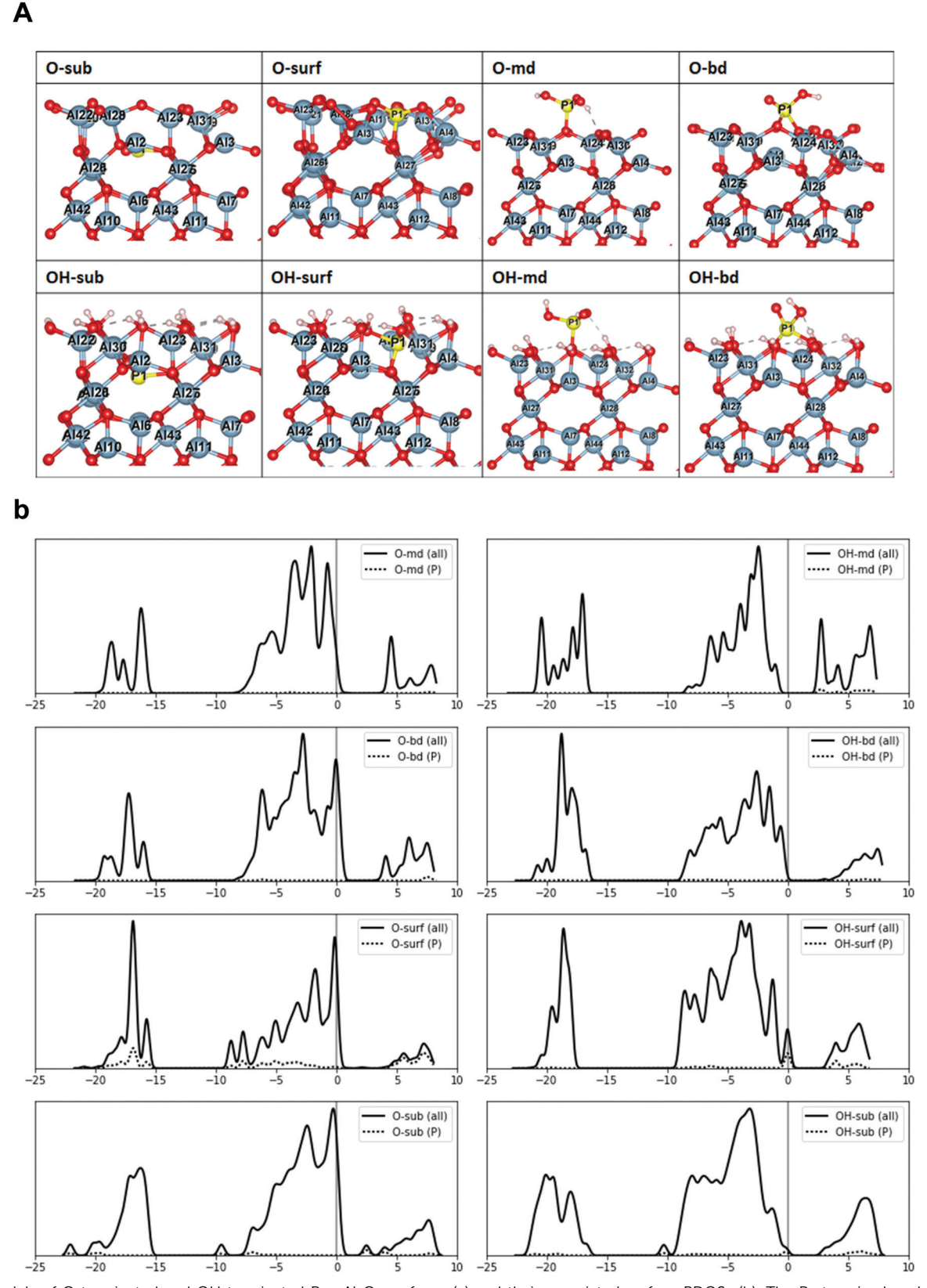


Fig. 2 Models of O terminated and OH terminated  $P-\gamma-Al_2O_3$  surfaces (a) and their associated surface PDOSs (b). The P atom is placed at various positions as defined before, particularly at the spinel defect site for **O-sub** and **OH-sub** models. In the PDOSs, the Fermi energy is set to zero. A clearer depiction of the tri-coordinated P atom in **O-surf** of inset (a) is found in Fig. S6 (ESI†).

16.0 nm b 400 mV 120.0 nm -500 mV 400 mV 400 mV

Fig. 3 (A and C) Topography and (B and D) potential mapping images of  $\gamma$ -Al<sub>2</sub>O<sub>3</sub> and P- $\gamma$ -Al<sub>2</sub>O<sub>3</sub> nanoparticles, respectively.

120.0 n

120.0 nm

surface dipole contributions ( $\phi_d$ ) are presented and compared with GGA quantities (see Table S1 for the entire set of calculated values, ESI†).

It is seen that for all surface models except **OH-md** and **OH-bd**, the computed WFs agree with the experiment in that WF is reduced as a result of P-doping. The reason for the fact that **OH-md** and **OH-bd** models stand out is complex and it involves two observations: (1) the surfaces do not rearrange significantly from the non-doped case and (2) the P-OH contribution to the surface dipole is to increase it. Specifically, comparing the P-OH angle and OH direction in **O-md** and **O-bd** with the

OH-counterparts from Fig. 2, we notice that the hydroxylated surfaces have a P-OH pointing upward, while the O-terminated surfaces have a P-OH pointing downward. Thus, when the phosphates are added to the surface, the dipole is depleted for the O-terminated surfaces and enhanced for the OH-terminated ones. This observation is especially important for the **OH-bd** system. When we inspect the effect of doping by two independent P atoms (higher concentration) on the WF for the various structures of subsurface (**O-sub** and **OH-sub**) models (see the Chart in S10a, ESI†), we notice that the addition of the second P atom further decreases the WF. Thus, theory and experiment semiquantitatively agree that on average P- $\gamma$ -Al<sub>2</sub>O<sub>3</sub> has a lower WF than non-doped  $\gamma$ -Al<sub>2</sub>O<sub>3</sub>, with the chemisorbed phosphate models going against the trend and increasing the WF values when the OH-terminated surfaces are considered.

To understand the reasons for the WF reduction by P doping we present in Fig. 4b the WF differences  $(\Delta\phi)$  between the non-doped and P-doped surfaces of each structural model, providing us with a comparison of theory and experimental results. It shows that all the O-terminated surfaces are in accordance with the experiment by yielding lower WF after P-doping (Fig. 4b). However, the dentate models (**OH-md** and **OH-bd**) increase the WF values.

The size of the surface dipole contribution to  $\phi$  ( $\phi_d$ ) estimated by computing the difference between the left and right vacuum levels<sup>32</sup> exhibits a clear trend that  $\phi_d$  reduces linearly with the increase in the number of P dopants for the O-terminated surfaces whereas it conversely rises for the OH-terminated surfaces (see Fig. S10b, ESI†).

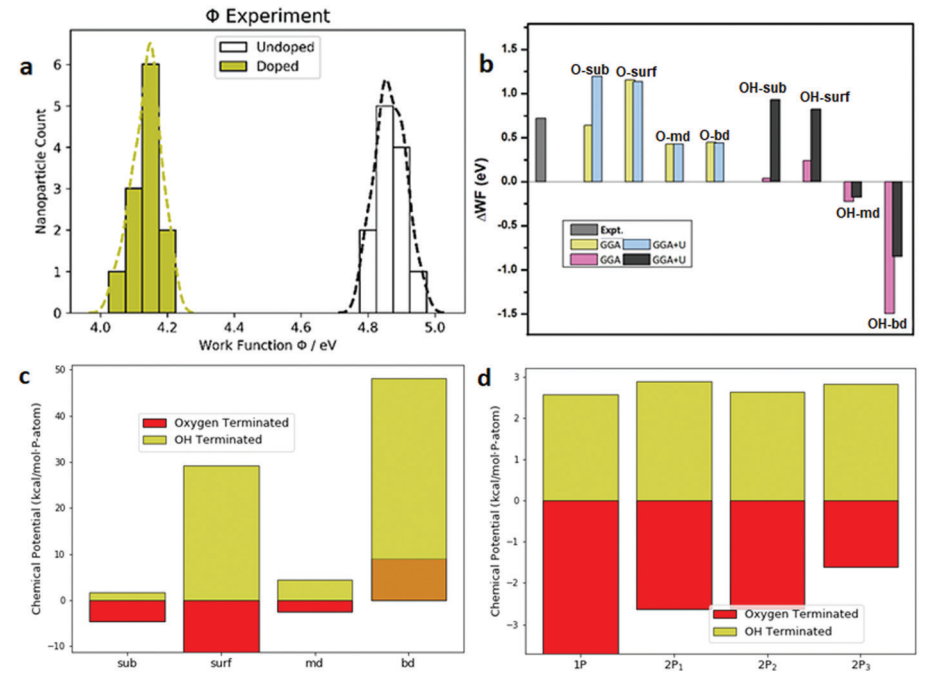


Fig. 4 (a) Experimentally determined WFs for non-doped and P-doped  $\gamma$ -Al<sub>2</sub>O<sub>3</sub>. (b) Comparison of the experimentally and theoretically determined WF differences ( $\Delta$ WF) between non-doped and P-doped structures for supercell models of O-terminated and OH-terminated surfaces. Here, the negative  $\Delta$ WF denotes the increase in WF after P-doping as opposed to experimental results. (c) Surface stability diagram of P doping in terms of the chemical potential for both O-terminated and OH-terminated surfaces. (d) Surface stability diagram of P doping (**O-sub** and **OH-sub** models) in terms of the chemical potential.  $2P_1$ ,  $2P_2$ , and  $2P_3$  are for three different available tetrahedral Al sites.

Our analysis is substantiated by characterizing the energetic stability of the O-/OH-terminated surfaces in terms of chemical potentials,  $\mu$  (see Fig. 4c), revealing that dentate attachment models on both O- and OH-terminated surfaces (**O-md/OH-md** and **O-bd/OH-bd**) are less stable compared to other surface models (**O-sub/OH-sub** and **O-surf/OH-surf**). Also, O-terminated surfaces are more stable than OH-terminated ones by providing **O-sub** models as the most stable ones among all possible configurations (Fig. 4d).

Furthermore, to get a structure-function relationship among various surface models of P-γ-Al<sub>2</sub>O<sub>3</sub> discussed here, we plot a correlation between the WF and  $\phi_d$  (Fig. S11, ESI†), which demonstrate the behavior of the electronic structure against the various P locations on γ-Al<sub>2</sub>O<sub>3</sub> surfaces. Fig. S11a (ESI†) shows that there exists a clear linear correlation between  $\phi$  and  $\phi_d$  for the models of O-terminated surfaces, whereas a less correlation for  $\phi - \phi_{\rm d}$  occurs for OH-terminated surfaces of supercells (Fig. S11b, ESI†). However, the similar plots for the small cell models (O- and OH-) (see Fig. S11c and d, ESI†) display a less linear correlation for O-terminated surfaces but a relatively good correlation for OH-terminated ones. This shows the importance of sizable finite size effects and surface relaxation effects on modeling of γ-Al<sub>2</sub>O<sub>3</sub> surfaces.<sup>33</sup> Upon inspection of the Bader charges of the P atom in O-terminated and OH-terminated surfaces, all varying between 0.14 and 0.17, we further confirm that the reduction in the WF witnessed in our simulations is due to a change in the dipole moment orientation rather than to charge transfer.

In order to obtain more detailed information about the structure and change in the chemical environment after P doping, the Al-NMR spectra were obtained for three samples; the as

received  $\gamma$ -Al<sub>2</sub>O<sub>3</sub>, P doped  $\gamma$ -Al<sub>2</sub>O<sub>3</sub> and heated  $\gamma$ -Al<sub>2</sub>O<sub>3</sub>, which were obtained by annealing γ-Al<sub>2</sub>O<sub>3</sub> at the same temperature as that applied for P doped  $\gamma$ -Al<sub>2</sub>O<sub>3</sub>, just without the H<sub>3</sub>PO<sub>4</sub> source (Fig. 5a). The spectrum of the as-received  $\gamma$ -Al<sub>2</sub>O<sub>3</sub> sample (in black) shows two peaks which correspond to AlO<sub>4</sub> at around 70 ppm and to AlO<sub>6</sub> at around 12 ppm with about 1:2 integration ratio, which is consistent with the values reported in the literature. 11,34,35 In the case of P-γ-Al<sub>2</sub>O<sub>3</sub>, the peak positions for AlO<sub>6</sub> and AlO<sub>4</sub> remain unchanged. While a new sharp peak appeared at 42.3 ppm and a shoulder to the octahedral Al peak appeared at around 4 ppm. The peak at 42.3 ppm has been assigned to AlO5 bonding. It is worth mentioning that the AlO5 surface units have been considered as selective anchoring sites for Pt catalysts.<sup>34</sup> The upshift of the shoulder is possibly caused by the coupling of P with the AlO<sub>6</sub> units to form Al-O-P in the local environment of the surface AlO<sub>6</sub> units.<sup>11</sup>

To assure that these structural changes are not due to a simple high temperature annealing effect, a control experiment was conducted, where the as-received  $\gamma\text{-Al}_2\text{O}_3$  was heated to 550 °C for 4.5 h (the same heating conditions as in the case of the P-doping process, without the phosphorus source). As shown in Fig. 5a, the heated  $\gamma\text{-Al}_2\text{O}_3$  shows a similar NMR spectrum to the as-received one,  $^{34}$  suggesting that the P-doping process promoted the structural rearrangement for the formation of so-called pentahedral coordination units (AlO $_5$ ) and possible Al–O–P structures.

Additional evidence supporting the experimental measurements for Al-NMR is provided by the theoretical calculations. Computations of bulk  $\gamma$ -Al<sub>2</sub>O<sub>3</sub> (carried out with GIPAW<sup>36</sup> on bulk  $\gamma$ -Al<sub>2</sub>O<sub>3</sub>) reproduce the experimental spectrum of the clean

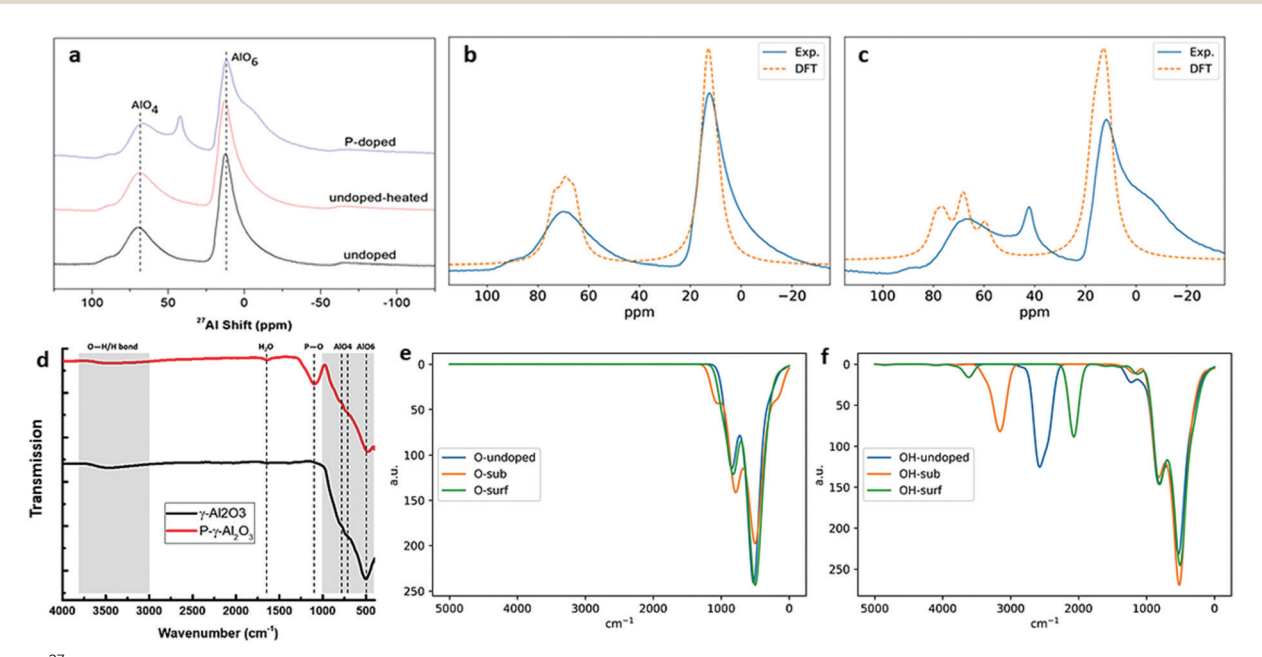


Fig. 5 (a)  $^{27}$ Al magic-angle spinning (MAS) NMR spectra of P-γ-Al<sub>2</sub>O<sub>3</sub> (top), heated γ-Al<sub>2</sub>O<sub>3</sub> (middle), and as received γ-Al<sub>2</sub>O<sub>3</sub> (bottom). Theoretical predictions of solid-state Al-NMR spectra computed on a bulk model supercell including 40 independent atoms and plotted with dashed lines; (b) non-doped γ-Al<sub>2</sub>O<sub>3</sub> and (c) P-doped γ-Al<sub>2</sub>O<sub>3</sub>. (d) Experimental IR spectra of the non-doped and P-doped γ-Al<sub>2</sub>O<sub>3</sub> nanoparticles. Calculated IR spectra (e) of subsurface (**O-sub**) and surface (**O-surf**) P-doped O-terminated surface models and (f) of subsurface (**OH-sub**) and surface (**OH-surf**) P-doped OH-terminated surface models.

non-doped γ-Al<sub>2</sub>O<sub>3</sub> nanoparticles with remarkable accuracy (Fig. 5b). The computational spectra (Fig. 5c) assign the peak at 42.3 ppm to either distorted tetrahedral or distorted octahedral-coordinated Al atoms. Our work, thus, improves upon recent theoretical results<sup>37</sup> which could only tentatively assign the 42.3 ppm peak to pentacoordinated Al atoms. We further find that the pentacoordinated Al atoms, depending on the nature of the bonding (lengths and angles), give rise to NMR peak upfield (not shown) compared to the octahedral Al atoms explaining the presence of the shoulder peak. It should be noted that our DFT calculations for the NMR computation of the P-doped surface structures did not converge. Our works on a comprehensive NMR computation of P-doped γ-Al<sub>2</sub>O<sub>3</sub> surface structures to accurately understand the shoulder at 0 ppm and the additional sharp peak at 42.3 ppm are in progress and will be published elsewhere.

To gain more information about the chemical bonds, both non-doped and P-doped γ-Al<sub>2</sub>O<sub>3</sub> nanoparticles were characterized with FT-IR spectroscopy (Fig. 5d). Also, we computed the vibrational frequencies for the models of O-terminated (Fig. 5e) and OH-terminated (Fig. 5f) γ-Al<sub>2</sub>O<sub>3</sub> surfaces. The experimental spectrum of γ-Al<sub>2</sub>O<sub>3</sub> shows a wide peak between 3000 and 3800 cm<sup>-1</sup>, which is assigned to O-H stretching and the hydrogen bond between the OH groups existing on the surface of Al<sub>2</sub>O<sub>3</sub>. <sup>38,39</sup> The computational spectra of all OH-terminated surface models and dentate models of O-terminated surfaces (O-md and O-bd) confirmed that the peaks in this region are due to the asymmetric stretching mode of O-H (see Fig. 5f and Fig. S12a, b, ESI†). The EDAX measurement indicated that the P loading in  $P-\gamma-Al_2O_3$  was around wt 8.5% (atomic 5.6%), which is much higher than those required to react all the surface hydroxy groups on the surface of  $\gamma$ -Al<sub>2</sub>O<sub>3</sub>. <sup>40,41</sup> However, this peak still exists, even though it is weakened in P- $\gamma$ -Al<sub>2</sub>O<sub>3</sub>. At the same time, the peak intensity is increased in P-γ-Al<sub>2</sub>O<sub>3</sub> at 1639 cm<sup>-1</sup>, which has been assigned to the bending moment of adsorbed water molecules. 42 The remaining weak peak is assigned to the hydroxy group stretching from surface phosphate groups formed upon P doping and/or from water molecules adsorbed on P-\gamma-Al2O3.40 On the other hand, the weak peak with a high P doping level also suggested that either some of the phosphate groups were dehydrated and/or some of the phosphorus was incorporated into the lattice of Al<sub>2</sub>O<sub>3</sub> (and not on the surface of the alumina). In the spectra of the OH-surf model, similar peaks, an intense peak at around 2000 cm<sup>-1</sup> and a relatively very small peak at around 1650 cm<sup>-1</sup> are reproduced due to the asymmetric stretching mode and inplane bending moments of O-H, respectively. A similar O-H bending mode is seen at around 2200 cm<sup>-1</sup> for the **OH-md** model (see Fig. S12b, ESI†).

Indeed, a significant peak at  $1100~\rm{cm}^{-1}$  appeared for  $P-\gamma-Al_2O_3$ , which was considered as the identification of different P–O stretching, especially for ideal tetrahedron  $[PO_4]^{3-}$  groups.  $^{12,43}$  However, our computational analysis shows that the **OH-non-doped** model also indicates such a peak and the peaks in this region result from the O–H bending mode for OH-terminated surface models of  $P-\gamma-Al_2O_3$ . Only the **O-sub** model has a peak due to P–O stretching in this region. For the other models, the

vibrational modes of P appear between 800 and 1000 cm<sup>-1</sup> as P–O bending mostly. This finding, in combination with the unexpected small peak of the hydroxy group of phosphate in the range of 3000–3800 cm<sup>-1</sup>, supports our hypothesis that P is either in the form of surface phosphate groups, which did not carry hydrogen atoms, and/or some of the P dopants incorporated inside the lattice or network of Al<sub>2</sub>O<sub>3</sub>.

It was reported that absorption in the range of 400-900 cm<sup>-1</sup> corresponds to the Al-O stretching related to the octahedral (AlO<sub>6</sub>) and tetrahedral (AlO<sub>4</sub>) units in the network of  $\gamma$ -Al<sub>2</sub>O<sub>3</sub>.<sup>44</sup> The FT-IR spectra of both γ-Al<sub>2</sub>O<sub>3</sub> and P-γ-Al<sub>2</sub>O<sub>3</sub> show absorptions in this range. More specifically, they all show peaks at 500 cm<sup>-1</sup> and two shoulders at 720 and 776 cm<sup>-1</sup>. The intensity of the peaks significantly decreases in P-γ-Al<sub>2</sub>O<sub>3</sub>, while the peak positions do not change very much. It was reported that Al-O stretching in AlO<sub>6</sub> and AlO<sub>4</sub> units was around 500-750 cm<sup>-1</sup> and 750-850 cm<sup>-1</sup>, respectively. The peak position may change significantly depending on the fabrication methods and existence of defects and dopants in the lattice of  $\gamma$ -Al<sub>2</sub>O<sub>3</sub>. 45 On the other hand, Du et al. reported that the bands at 523 and 570 cm<sup>-1</sup> are related to the stretching mode of Al-O in AlO<sub>6</sub> and  $AlO_4$ , respectively. The bands at 734 and 774 cm<sup>-1</sup> are related to the symmetric stretching vibration of the AlO<sub>4</sub> tetrahedron.<sup>44</sup> Boumaza et al. reported that Al-O stretching in AlO<sub>6</sub> was 491 cm<sup>-1</sup>.46 Based on these literature reports, the peak at 500 cm<sup>-1</sup> is assigned to Al-O stretching in the octahedral units  $(AlO_6)^{46,47}$  and the shoulders at 720 cm<sup>-1</sup> and 776 cm<sup>-1</sup> are related to the symmetric stretching vibration of the AlO<sub>4</sub> tetrahedron. 44,48 The relative decrease in these peaks upon P doping in this range might be due to the decrease of their population upon introducing phosphorus into the Al<sub>2</sub>O<sub>3</sub> lattice or due to the formed PO<sub>4</sub> species covered on the surface, which decreases the detectable absorption of these bands. These results are confirmed by the presence of some P related vibrational modes seen at around 700 cm<sup>-1</sup> and 500 cm<sup>-1</sup> in both O/OH-terminated surface models. Overall, our computational approach is able to reproduce the main features of the experimental spectra, especially for OH-sub and OH-surf models.

## Conclusions

In conclusion, employing experimental and computational methods, we have shown that the electronic properties of metal oxide surfaces can be manipulated *via* group 5A doping (P atoms in this work). The surfaces can be made electron-rich in the sense that they have a lower work function than the undoped ones. The main reason for the lowering of the work function is the introduction of a surface dipole after doping. Interestingly, we find that the OH groups of thermodynamically stable mono- and bi-dentate phosphate surface ligands cooperate with the surface by damping its dipole thereby decreasing the work function. Substitutional P-doping leads to nonsymmetric arrangements of P (triand four-coordinated) with an added dipole that once again dampens the work functions. The reduced coordination of the P atom correlates with the reported higher catalytic activity

of P-doped alumina surfaces. With this study, we paved the way to use group 5A doping as a tuning knob for engineering the electrostatic properties of metal oxide surfaces with catalytic applications.

Materials and methods

#### Preparation of samples

**Paper** 

Doping γ-Al<sub>2</sub>O<sub>3</sub> (Sigma Aldrich, gamma phase aluminum oxide nanopowder) with P was achieved by impregnation of γ-Al<sub>2</sub>O<sub>3</sub> with phosphoric acid (with a ratio of 14 g of γ-Al<sub>2</sub>O<sub>3</sub> per 100 mL of 1.0 M phosphoric acid, Sigma Aldrich, 85 wt% in H<sub>2</sub>O) for 7 h while stirring to reach equilibrium adsorption.<sup>49</sup> After impregnation, the sample was dried at 100 °C overnight, and then was placed in an oven at 550 °C for 4.5 h. The product was then sonicated and dispersed in ultrapure water and centrifuged 5 times at 5000 rpm for 8 min, to make sure that there is no free phosphoric acid in the sample. The final product was then dried at 100 °C overnight.

#### Characterization

PF-KPFM measurements on the alumina samples were conducted with a Dimension ICON AFM setup inside an argon-filled glove box where both H<sub>2</sub>O and O<sub>2</sub> levels were below 0.1 ppm. The probes used were PFQNE-AL (Bruker AFM Probes), composed of a silicon nitride cantilever with a sharp silicon tip. The highly inert environment helped us to conduct more accurate measurements.  $P-\gamma-Al_2O_3$  and  $\gamma-Al_2O_3$  particles were first dispersed into ethanol, using bath sonication for 3 minutes. Then the samples were prepared by drop casting the dispersion of P-γ-Al<sub>2</sub>O<sub>3</sub> and γ-Al<sub>2</sub>O<sub>3</sub> particles onto a boron-doped silicon substrate. Solid state <sup>27</sup>Al (130.2 MHz) magic-angle spinning (MAS) NMR spectra were acquired at a magnetic field of 11.74T with a Bruker Avance III HD spectrometer equipped with a 4 mm solid-state broadband probe (Bruker Biospin, Billerica, MA). One-pulse spectra were recorded with 45 deg pulse of 1 µs and 0.4 s relaxation delay, collecting 1 K data points over 104 kHz with the sample spinning at 10 kHz in a 4 mm zirconia rotor, in which the finely powdered samples were packed. The FT-IR spectra of  $\gamma$ -Al<sub>2</sub>O<sub>3</sub> and P- $\gamma$ -Al<sub>2</sub>O<sub>3</sub> were acquired with a Thermo-Nicolet iS5 spectrometer (Thermo-Electron Corp., Madison, WI), using an iD7 ATR accessory with a diamond crystal plate, in the range of 400 to 4000 cm<sup>-1</sup>. The spectra were recorded after 16 scans with a resolution of 4 cm<sup>-1</sup>.

#### Computational details

Our simulations relied on Density Functional Theory (DFT), and specifically we employ the Quantum ESPRESSO software. 50 In the calculations, the PBE functional<sup>51</sup> and Projector Augmented Wave (PAW) Pseudopotentials were employed with a kinetic energy cutoff of 50 Ry for the wavefunctions and a kinetic energy cutoff of 500 Ry for the charge density and potential. A Gaussian smearing to the occupations of the KS states was used, with a width (sigma) of 0.0001 Ry.50 The self-consistent field calculations featured a Broyden mixing beta of 0.15. A k-point sampling on a  $2 \times 2 \times 1$ grid of points for geometry optimizations and a  $4 \times 4 \times 1$  grid

for all single-point computations were set.<sup>52</sup> Additional nonself-consistent field (NSCF) was employed to generate smoother DOS plots.

The NMR calculations were carried out on the optimized bulk γ-Al<sub>2</sub>O<sub>3</sub> structures by first performing a self-consistent field (SCF) calculation with pw.x. Computation of NMR spectra has been carried out using the DFT GIPAW (The Gauge-Including Projector Augmented Wave)<sup>36</sup> method using norm-conserving PPs (e.g. Al.pbe-tm-gipaw-dc.UPF) with the PBE functional.

IR spectra calculations were computed with PHONON<sup>49</sup> to generate vibrational frequencies and carried out with fixed occupations (no smearing). In these calculations we first performed a SCF calculation with pw.x, second, we calculated the vibrational frequencies (normal modes/phonons) with ph.x and finally using dynmat.x we collected the phonon information from ph.x output. The wavefunction kinetic energy cutoff for phonon calculation was 50 Ry on a  $4 \times 4 \times 1$  k-point grid with  $1.0 \times 10^{-14}$  threshold.

The chemical potentials  $(\mu)$  were calculated as follows: For P-doped and surface models (O-sub, O-surf, OH-sub, and OH-surf):

$$\mu_{\text{P-doped/surface}} = E_{\text{P-doped-}\gamma\text{-Al}_2\text{O}_3} - E_{\gamma\text{-Al}_2\text{O}_3} + (E_{\text{Al}} - E_{\text{P}})$$
 (1)

For monodentate (O-md and OH-md) and bidentate models (O-bd and OH-bd):

$$\mu_{\text{monodentate}} = E_{\text{P-doped-}\gamma\text{-Al}_2\text{O}_3} - E_{\gamma\text{-Al}_2\text{O}_3} - E_{\text{H}_3\text{PO}_4} + E_{\text{H}} + E_{\text{O}}$$
(2)

$$\mu_{\rm bidentate} = E_{\text{P-doped-}\gamma\text{-Al}_2{\rm O}_3} - E_{\gamma\text{-Al}_2{\rm O}_3} - E_{{\rm H}_3{\rm PO}_4} + 2E_{\rm H} + 2E_{\rm O} \end{(3)}$$

where the energy values were computed using the same cell for all species.

## Conflicts of interest

There are no conflicts to declare.

## Acknowledgements

This material is based on work supported by the National Science Foundation under Grant DMR-1742807 and ACS Petroleum Research Fund under grant 58557-ND5. Work function studies with a Kelvin Probe Microscope were supported by NSF MRI 1429062.

## References

- 1 Y. P. Gavin Chua, G. T. Kasun Kalhara Gunasooriya, M. Saeys and E. G. Seebauer, J. Catal., 2014, 311, 306-313.
- 2 L. Li, Y. Zhang, A. M. Schultz, X. Liu, P. A. Salvador and G. S. Rohrer, Catal. Sci. Technol., 2012, 2, 1945-1952.
- 3 N. K. Nandakumar and E. G. Seebauer, J. Phys. Chem. C, 2014, 118, 6873-6881.
- 4 M. Chiesa, E. Giamello, D. M. Murphy, G. Pacchioni, M. C. Paganini, R. Soave and Z. Sojka, J. Phys. Chem. B, 2001, 105, 497-505.

5 P. Gorai, Y. V. Kondratenko and E. G. Seebauer, J. Appl.

- Phys., 2012, 111(9), 094510.
- 6 M.-G. Ma, Y.-J. Zhu and Z.-L. Xu, Mater. Lett., 2007, 61(8), 1812-1815.
- 7 Y. Rozita, R. Brydson and A. J. Scott, J. Phys.: Conf. Ser., 2010, 241(1), 012096.
- 8 J. B. Peri, J. Phys. Chem., 1965, 69, 220-230.
- 9 W. Gu, M. Shen, X. Chang, Y. Wang and J. Wang, J. Alloys Compd., 2007, 441, 311-316.
- 10 Y. Wang, J. Wang, M. Shen and W. Wang, J. Alloys Compd., 2009, 467, 405-412.
- 11 J. Wang, Y. Wang, J. Wen, M. Shen and W. Wang, Microporous Mesoporous Mater., 2009, 121, 208-218.
- 12 G. H. Mekhemer, A. K. H. Nohman, N. E. Fouad and H. Khalaf, Colloids Surf., A, 2000, 161, 439-446.
- 13 G. Busca, G. Ramis, V. Lorenzelli, P. F. Rossi, A. La Ginestra, D. Chimica, R. La, P. A. Mor and P. Patron, Langmuir, 1989, 5, 911-916.
- 14 P. Da Costa, C. Potvin, J. M. Manoli, M. Breysse and G. Djéga-Mariadassou, Catal. Lett., 2001, 72, 91-97.
- 15 K. Gishti, A. Iannibello, S. Marengo, G. Morelli, P. Tittarelli and V. Bassini, Appl. Catal., 1984, 12, 381-393.
- 16 K. H. Zum Gahr, Wear, 1996, 200, 215-224.
- 17 H. R. Pasaribu, J. W. Sloetjes and D. J. Schipper, Wear, 2003, 255, 699-707.
- 18 T. Ishizaka, R. Nozaki and Y. Kurokawa, J. Phys. Chem. Solids, 2002, 63, 613-617.
- 19 O. Ozuna, G. A. Hirata and J. McKittrick, Appl. Phys. Lett., 2004, 84, 1296-1298.
- 20 J. Zhang, Y. Wu, M. Xing, S. A. K. Leghari and S. Sajjad, Energy Environ. Sci., 2010, 3, 715-726.
- 21 R. Li, Z. Wei, X. Gou and W. Xu, RSC Adv., 2013, 3, 9978-9984.
- 22 C. H. Choi, M. W. Chung, S. H. Park and S. I. Woo, Phys. Chem. Chem. Phys., 2013, 15, 1802-1805.
- 23 A. K. Khattak, K. Mahmood, M. Afzal, M. Saleem and R. Qadeer, Colloids Surf., A, 2004, 236, 103-110.
- 24 M. Villarroel, P. Baeza, F. Gracia, N. Escalona, P. Avila and F. G. Gil-Llambias, Appl. Catal., A, 2009, 364, 75-79.
- 25 J. Quartararo, J. P. Amoureux and J. Grimblot, J. Mol. Catal. A: Chem., 2000, 162, 353-365.
- 26 G. Gutiérrez, A. Taga and B. Johansson, Phys. Rev. B: Condens. Matter Mater. Phys., 2001, 65, 012101.
- 27 H. P. Pinto, R. M. Nieminen and S. D. Elliott, Phys. Rev. B: Condens. Matter Mater. Phys., 2004, 70, 125402.
- 28 T. Taniike, M. Tada, Y. Morikawa, T. Sasaki and Y. Iwasawa, J. Phys. Chem. B, 2006, 110, 4929-4936.
- 29 G. Paglia, C. E. Buckley, A. L. Rohl, R. D. Hart, K. Winter, A. J. Studer, B. Hunter and J. V. Hanna, Chem. Mater., 2004, 16, 220-236.
- 30 M. Cococcioni and S. de Gironcoli, Phys. Rev. B: Condens. Matter Mater. Phys., 2005, 71, 035105.

- 31 E. Finazzi, C. Di Valentin, G. Pacchioni and A. Selloni, I. Chem. Phys., 2008, 129, 154113.
- 32 D. Cornil, H. Li, C. Wood, G. Pourtois, J. Brédas and J. Cornil, ChemPhysChem, 2013, 14, 2939-2946.
- 33 M. Acikgoz, J. Harrell and M. Pavanello, J. Phys. Chem. C. 2018, 122(44), 25314-25330.
- 34 N. S. Barrow, A. Scullard and N. Collis, Johnson Matthey Technol. Rev., 2016, 60(2), 90.
- 35 L. Samain, A. Jaworski, M. Edén, D. M. Ladd, D. K. Seo, F. Javier Garcia-Garcia and U. Häussermann, J. Solid State Chem., 2014, 217, 1-8.
- 36 J. R. Yates, C. J. Pickard and F. Mauri, Phys. Rev. B: Condens. Matter Mater. Phys., 2007, 76, 024401.
- 37 R. Wischert, P. Florian, C. Copéret, D. Massiot and P. Sautet, I. Phys. Chem. C, 2014, 118(28), 15292-15299.
- 38 S. Wang, X. Li, S. Wang, Y. Li and Y. Zhai, Mater. Lett., 2008, 62(20), 3552-3554.
- 39 H. A. Dabbagh, M. Yalfani and B. H. Davis, J. Mol. Catal. A: Chem., 2005, 238(1), 72-77.
- 40 E. C. Decanio, J. C. Edwards, T. R. Scalzo, D. A. Storm and J. W. Bruno, J. Catal., 1991, 132(2), 498-511.
- 41 S. Sigurdson, V. Sundaramurthy, A. K. Dalai and J. Adjaye, J. Mol. Catal. A: Chem., 2008, 291(1), 30-37.
- 42 T. Meher, A. K. Basu and S. Ghatak, Ceram. Int., 2005, 31(6), 831-838.
- 43 M. Rokita, M. Handke and W. Mozgawa, J. Mol. Struct., 1998, 450(1), 213-217.
- 44 X. Du, Y. Wang, X. Su and J. Li, Powder Technol., 2009, 192(1), 40-46.
- 45 R. Rinaldi and U. Schuchardt, J. Catal., 2005, 236(2), 335–345.
- 46 A. Boumaza, L. Favaro, J. Lédion, G. Sattonnay, J. B. Brubach, P. Berthet, A. M. Huntz, P. Roy and R. Tétot, J. Solid State Chem., 2009, 182(5), 1171-1176.
- 47 M. N. Barroso, M. F. Gomez, L. A. Arrúa and M. C. Abello, Catal. Lett., 2006, 109(1), 13-19.
- 48 X. L. Qi, Z. Wang, S. J. Li, B. Li, X. Y. Liu and B. X. Lin, Acta Phys.-Chim. Sin., 2006, 22(2), 198-202.
- 49 R. Iwamoto and J. Grimblot, Adv. Catal., 1999, 44, 417-503.
- 50 P. Giannozzi, S. Baroni, N. Bonini, M. Calandra, R. Car, C. Cavazzoni, D. Ceresoli, G. L. Chiarotti, M. Cococcioni, I. Dabo, A. Dal Corso, S. de Gironcoli, S. Fabris, G. Fratesi, R. Gebauer, U. Gerstmann, C. Gougoussis, A. Kokalj, M. Lazzeri, L. Martin-Samos, N. Marzari, F. Mauri, R. Mazzarello, S. Paolini, A. Pasquarello, L. Paulatto, C. Sbraccia, S. Scandolo, G. Sclauzero, A. P. Seitsonen, A. Smogunov, P. Umari and R. M. Wentzcovitch, J. Phys.: Condens. Matter, 2009, 21, 395502.
- 51 J. P. Perdew, K. Burke and M. Ernzerhof, Phys. Rev. Lett., 1996, 77(18), 3865-3868.
- 52 H. J. Monkhorst and J. D. Pack, Phys. Rev. B: Solid State, 1976, 13, 5188.